Local structural changes in $Ce_{1-x}Ln_xO_{2-\delta}$ (Ln = La, Gd) solid electrolytes

Xue Liu[1], Runosuke Minato[1], Yasumasa Otani[1], Kengo Hatai[1], Kei-ichiro Murai[1], Masashi Mori[2], Atsushi Yoshinari[3], Munehiko Miyano[3], Atsushi Sakaki[3] and Toshihiro Moriga[1]*

[1]*Graduate School of Advanced Technology and Science, Tokushima University, Tokushima 770-8506, Japan*

[2] *Central Research Institute of Electric Power Industry, Yokosuka 240-0196, Japan*

[3]*R&D Division, NICHIA Corporation*
Anan, Tokushima 774-8601, Japan

* Corresponding Author E-mail: moriga@tokushima-u.ac.jp

Abstract

The local structural changes in La and Gd in doped ceria were investigated using the XAFS technique. In addition, $Ce_{1-x}Ln_xO_{2-\delta}$ (Ln = La, Gd; LDC) ($0 \leq x \leq 0.5$) was synthesized through a coprecipitation method and the local structures were analyzed based on the XAFS spectra for the first and second neighbor shells of the constituent cations. For these two types of materials, the variation in the coordination number of the Ln and Ce cations showed different trends as a function of the dopant concentration, x. For LDC, a local structural ordering was formed at $x \geq 0.3$ similar to a pyrochlore-type structure, in which the oxygen vacancies are preferentially located adjacent to La^{3+}. For $Ce_{1-x}Gd_xO_{2-\delta}$ (GDC), no distinct differences in the coordination number of the cations were observed.

The combined XAFS and XRD results successfully showed that the weighted average distances of the longer Ln-Ln (Ln = La for LDC and Ln = Gd for GDC) and shorter Ce-Ce at each composition, as obtained through XAFS analysis, fit extremely well with the lattice parameter obtained using XRD. A model of the local structural change was derived to explain the variation in the electrical conductivity during the early stage of Ln doping.

1. Introduction

Solid oxide fuel cells (SOFCs), which are one of the most versatile clean energy technologies, have been of interest for achieving a high efficiency in converting chemical to electrical energy in recent years[1]. Their function is to produce oxygen anions through the molecular O_2 reaction with electrons at the cathode. The oxygen anions can then be transported through an oxide ion-conducting electrolyte to the anode interface via an oxygen vacancy compensation mechanism[2, 3]. The electrolyte plays an important role in a SOFC, and generally requires a dense structure, low electronic conductivity, high ionic conductivity, excellent chemical stability with the fuel, oxidant and electrode materials, and a small mismatch between its thermal expansion coefficient and those of the electrodes[4].

Ceria-based mixed oxide is one of the most important electrolyte materials available and has numerous applications[5]. For example, it has been reported that La^{3+} in Au/CeO_2-La_2O_3 yields an improved catalytic activity for NO reduction[6]. This is based on ceria doping with other rare-earth oxides, which has attracted significant attention for medium-temperature electrolytes used to increase the oxygen storage capacity and have a high oxide conductivity in the range of 500 °C to 700 °C [7]. The latter makes the electrolytes stable and easy to prepare.

From previous studies, elements Gd and Sm, when doped in ceria, are considered to provide better performance than other elements[8-12]. In addition, it has been reported that $Gd_{0.1}Ce_{0.9}O_{1.95}$ (x = 0.1 in $Ce_{1-x}Gd_xO_{2-\delta}$, GDC) shows the highest oxide ionic conductivity with different levels of dopants within the temperature range of 500 °C to 700 °C[13]. However, the high cost of these two rare elements makes them difficult to apply globally.

The pursuit of low manufacturing costs has therefore stimulated research for other alternatives.

Some researchers have focused on La or Y because they are inexpensive and can provide a similar performance as Gd or Sm. In addition, La doped in ceria for SOFCs can lower the reaction temperature compared to other elements[14].

According to a previous study, the electrical conductivity is related to the calcination temperature. Otherwise, the electrical conductivity of $Ce_{1-x}La_xO_{2-\delta}$ (LDC) shows a specific behavior at $x = 0.3$. Typically, the conductivity of a ceria-type material is highest at $0.1 \leq x \leq 0.2$, and continues to decrease with an increase in the amount of La[15]. However, as Figure 1 indicates, the conductivity of LDC shows an increasing trend again from $x \geq 0.3$. Other studies indicate that the electrical conductivity changes with the local structure[16, 17]. For example, oxygen ordering in a rare earth C-type oxide was detected in $La_2Ce_2O_7$. The composition of $La_2Ce_2O_7$ is nominally associated with the pyrochlore-type structure, which can be considered as an ordered defect fluorite-type structure. Assuming $Ln_2Ce_2O_7$ has a pyrochlore-type structure, the coordination number of the larger Ln^{3+} ion is 8, whereas that for the smaller Ce^{4+} ion is 6, indicating that a disproportion in the coordination numbers occurs due to a difference in cation sizes. In the case of zirconates, the electrical conductivity in $Ln_2Zr_2O_7$ increases with an increase in the ionic radius of Ln^{3+} in the fluorite-type phase region, and is finally the maximum in the vicinity of the phase boundary in the pyrochlore-type region. Therefore, we surmise that a local structural change also occurred in our target materials.

In this study, we introduce La and Gd individually into ceria to study the local structural change. The ionic radii of La^{3+} with 6-, 7-, and 8-fold coordination are 1.032 Å, 1.1 Å, and 1.16 Å, respectively. The ionic radii of Ce^{4+} with 6- and 8-fold coordination are 0.87

Å and 0.97 Å, while those of Gd^{3+} with 6-, 7-, and 8-fold coordination are 0.938 Å, 1 Å, and 1.053 Å, respectively[18]. We conducted XAFS to analyze the results. Based on the results, we obtained the regularities of the materials with different levels of doped La and Gd as well as the relationship between the conductivity and local structural changes. The proposed method aims to be a practical approach for solving structural problems in the future.

2. Experimental

2.1 Sample synthesis

We synthesized samples of $Ce_{1-x}La_xO_{2-\delta}$ ($0 \leq x \leq 0.5$) for XAFS measurements using the nanoparticle growth method, which is a type of coprecipitation method[19]. First, we weighed the starting materials i.e. $Ce(NO_3)_3 \cdot 6H_2O$ (99.99% purity, manufactured by Wako Pure Chemical Industries, Ltd.) and $La(NO_3)_3 \cdot 6H_2O$ (99.0% purity, manufactured by Wako Pure Chemical Industries, Ltd.) stoichiometrically, and dissolved them into 100 mL of deionized water. The solution was stirred and heated up to 80 °C. Subsequently, NH_4HCO_3 (99.99% purity, manufactured by Kanto Kagaku Co., Ltd.) was weighed and dissolved into 100 mL of deionized water as a precipitating reagent. Then, we added the reagent dropwise to a metal ion solution to form a precipitate. After 3 h with stirring at 80 °C, the precipitate was filtered and collected. Next, we placed the precipitate in a drying oven at 100 °C overnight to remove the water completely. The dried sample was disintegrated for 15 min using an agate mortar and then fired at 600 °C for 1 h. The calcined sample was disintegrated again and mixed in a rotary ball mill using zirconia balls with ethanol as a medium for 72 h and dried again. The sample was then ground for

5 min in an agate mortar. After grinding, the sample was uniaxially pressed into a 13 mm disk pellet at 30 MPa for 2 min. The pellets were then sintered at 1,500 °C for 5 h in air, following which the color of the pellets changed to grey.

Synthesis of the Gd-doped CeO_2 powder $Ce_{1-x}Gd_xO_{2-\delta}$ ($0 \leq x \leq 0.5$) was also carried out using the same procedure and $Gd(NO_3)_3 \cdot 6H_2O$ (Wako Pure Chemical Industries, Ltd., 99.95% or higher purity) as the starting material.

2.2 XAFS measurements and analysis

XAFS measurements of the La- and Gd-doped ceria were conducted at the BL16B2 beamline of the Spring-8 synchrotron facility in Japan. An aspirate amount of doped ceria was mixed with hexagonal boron nitride powder and uniaxially pressed into a 10 mm pellet for measurement. XAFS spectra near the Ce K-edge (40.45 keV), La K-edge (38.94 keV), and Gd K-edge (50.24 keV) were measured using the transmission mode at room temperature. In addition, CeO_2, La_2O_3, and Gd_2O_3 were measured as reference samples. An X-ray was monochromatized using a Si(311) double-crystal monochromator. A cylindrical Rh-coated mirror was used for elimination of the higher harmonics. Ionization chambers were filled with Ar-diluted Kr gas (Ar:Kr = 75%:25%) for measuring the incident X-ray and pure Kr gas for the transmitted X-ray, respectively.

The XAFS spectra were analyzed for both the first and second neighbor shells. Athena software was used to analyze the XAFS oscillation extraction, and Artemis was used for the curve-fitting of the XAFS oscillation[20]. The XAFS analysis conditions and parameters obtained are summarized in Tables 1 and 2, respectively. The k-range used for obtaining the radial distribution functions for each absorbing atom (in Figure 4) was basically fixed from 3 to 13 $Å^{-1}$. Curve-fitting was applied against the r-range from

approximately 1.4 to 2.1 Å for the first neighbors and from 2.8 to 4.1 Å for the second neighbors.

When we analyzed the distance between the La-absorbing atoms in the second neighbor shell, we assumed that the distances are mainly characterized by two types of coordination. One is La-La and the other is La-Ce. Because La has a larger ionic radius than Ce, when the two types of bonds mentioned are obtained in the second neighbor shell, the longer one is attributable to La-La and the shorter one to La-Ce. The coordination numbers of La and Ce are distributed according to the cation composition. In a similar manner, the two types of coordination in the second neighbor of Ce and Gd were assumed based on the fact that the ionic radius decreases in the following manner: La^{3+} (1.16 Å in 8-fold coordination) > Ce^{4+} (1.143 Å in 8-fold coordination) > Gd^{3+} (1.053 Å in 8-fold coordination)[21].

3. Results and discussion

According to a previous study, the solubility limit of Gd in the fluorite-type structure is within the compositional range of $0.4 < x < 0.5$[22]. It was also demonstrated that peaks assigned to the rare earth oxide C-type Gd_2O_3 appear when x reached 0.5. However, as shown in the powder X-ray diffraction patterns for $Ce_{1-x}La_xO_{2-\delta}$ ($0 \leq x \leq 0.5$), LDC, $Ce_{1-x}La_xO_{2-\delta}$ ($0 \leq x \leq 0.5$), and GDC, no impurities were contained in these samples. One possible reason for the difference might be the different firing temperatures. The GDC samples used in this experiment were fired at 1,500 °C, whereas those in the study mentioned[22] were fired at 1,300 °C. The higher temperature leads to a more disordered atomic arrangement in the lattice, and the C-type structure can be considered as the

superstructure of the fluorite-type structure. The oxygen deficiency might also be affected by the firing temperature.

Figure 2 shows the lattice parameters of the LDC and GDC with increasing doping amounts of La and Gd, respectively. For both LDC and GDC, the lattice parameters increased gradually with the amount of doped Ln. The changes in the lattice parameters in LDC were distinct and greater than those in GDC. In the curve of the lattice parameters for LDC, the trend of change as a function of x was similar to previously reported results[23], although the values were slightly different. Interestingly, the lattice constants increased linearly with an increase in x, but with a bend point at x = 0.4. Thus, we consider that there is a drastic structural change in the LDC composition between x = 0.3 and x = 0.4.

The increase in the lattice parameters for GDC with an increase in the doping amount is not as distinct as that for LDC. In the curve of the lattice parameters for GDC, the trend of change in the value is similar to previously reported results [23, 24]. The change is extremely smooth, and no abrupt changes in the compositional dependence of the lattice parameters are detected. Our data were in the range of results obtained by studies in the specific literature. Some previous results have reported that the local structure changes from fluorite-type to a rare earth C-type with $x \geq 0.4$[22]. Thus, we consider that there may be different structural changes in LDC and GDC.

Figure 3 shows the absorption spectra near the Ce K-edge and La K-edge in LDC, as well as near the Ce K-edge and Gd K-edge in GDC. The energy of the absorption edge is related to the electronic state of the X-ray absorbing cations. From the Ce K spectra of the LDC and GDC, we can observe that the peak position of the absorption edge does not clearly change with an increase in the amount of dopant. This indicates that in both LDC

and GDC, most of the CeO_2 valence is 4+ and does not change to 3+ as the amount of Ln doping increases. The structural change is not caused by the change in the Ce valence. Nolan claimed that a reduction of Ce^{4+} to Ce^{3+} in La-doped CeO_2 is preferably caused by the introduction of La^{3+}[25]. However, neither a peak shift nor a change in shape were observed in the spectra.

Figure 4 shows the peaks of the radial structural functions of the Ce K absorption edge and La K absorption edge in LDC, and the Ce K absorption edge and Gd K absorption edge in GDC. In LDC, the peak representing the first close distance of the Ce K absorption edge graph shifted to the left as the La doping amount increased, and the peak of the second proximity distance also shifted slightly to the left. By contrast, the graph of the La K absorption edge showed almost no change in position even when the La doping amount increased. This suggests that the coupling length around Ce decreases, while that around La does not change. However, in GDC, all peaks of the Ce K absorption edge and Gd K absorption edge shifted to the left as the amount of Gd doping increased. From this result, it is conceivable that all coupling lengths around Ce and Gd decreased.

Figure 5 shows the curves of the Ln-O inter atomic distance in $Ce_{1-x}Ln_xO_{2-\delta}$ ($0 \leq x \leq 0.5$) (Ln = La, Gd). These curves were calculated using the first shell of the XAFS results. From these curves, we can notice that the La-O distance increases slightly to approximately 2.460 Å below x = 0.4, and decreases slightly to 2.448 Å at x = 0.5. The sum of the ionic radii of 7-fold La^{3+} and 4-fold O^{2-} is 2.480 Å, and that of 6-fold La^{3+} and 4-fold O^{2-} is 2.412 Å[23], as indicated on the right side of Figure 5. Overall, the distances remained constant with the 7-fold coordination of La, whereas the distances of Ce and O clearly changed from 2.353 Å at x = 0 to 2.270 Å at x = 0.5. The sum of the ionic radii of 8-fold Ce^{4+} and 4-fold O^{2-} is 2.350 Å and that of 6-fold Ce^{4+} and 4-fold O^{2-} is 2.250 Å.

This indicates that Ce changed from a 7-fold coordination to a 6-fold coordination on average.

According to the analysis shown in Figure 3, there is no valence change in the local structure. We therefore consider that, as the factors affecting the Ce coordination change, oxygen vacancies are introduced due to the doped La. In addition, the oxygen vacancies are completely surrounded with Ce^{4+}.

By contrast, for GDC, the distance between Ce and O changed identically with that in the LDC. This indicates that the Ce changed from a 7-fold coordination to a 6-fold coordination on average, similarly to LDC. However, for the Gd and O pair, the distance decreased simultaneously with that of Ce and O, which changed from 2.391 to 2.346 Å. These Gd-O distances are close to the sum of the ionic radii of 8-fold Gd^{3+}, 7- or 6-fold Gd^{3+}, and 4 fold O^{2-}, which are 2.433, 2.380, and 2.318 Å, respectively. This indicates that some of the coordination of Gd changed from 7- to 6-fold on average. We consider the main factor for the coordination change to be the numerous oxygen vacancies occurring in GDC. The oxygen vacancies are statistically introduced and surround Ce^{4+} and Gd^{3+}. It can also be observed from Figure 5 that, with the amount of doped La and Gd, the gap in the Ce-O distance in LDC and GDC gradually increases. This is caused by the number of oxygen vacancies surrounding Ce^{4+} and supports our conclusion.

There are usually two factors affecting the distance between the cations and oxygen, i.e., the cation coordination number and valence (giving the bond strength according to Pauling)[26]. For LDC, the radius of La^{3+} with a 7-fold coordination is much larger than that of Ce^{4+} with 8- and 6-fold coordination. However, the valence of La is lower than that of Ce. In LDC, the coordination of La is a constant 7-fold in the range of x = 0.1 to 0.5, whereas the coordination of Ce gradually decreases almost linearly from 8 to 6.3.

This implies that the contribution of the valence to the distance between La and O is higher than that of the radius. The ability of La to catch up with O^{2-} is higher than that of Ce, and it can maintain the stability of the local La-O structure. Thus, the oxygen vacancies are surrounded with Ce^{4+} instead of La^{3+}. Unlike fluorite-type and the usual pyrochlore-type structure, La has a 7-fold coordination. Thus, the local cubic structure cannot completely maintain the fluorite-type structure or a pyrochlore-type structure with an increase in La. We believe that it forms a superstructure that is more like a pyrochlore-type structure in LDC at x = 0.3. By contrast, for GDC, the size of the 6-fold coordination of Gd^{3+} is similar to that of the 8-fold coordination of Ce^{4+}. The Gd coordination gradually decreases at the same pace as the Ce coordination. The ability of Gd to catch up with O^{2-} is the same as that of Ce, and hence, it cannot maintain a stable local Gd-O structure. This is the reason why the oxygen vacancies are statistically distributed around Ce^{4+} and Gd^{3+}. In a rare earth C-type structure, Gd^{3+} has a 6-fold coordination, and in a fluorite-type structure, a 6-or 7-fold coordination is considered. Hence it is thought that the coordination number does not change significantly even if the doping amount of Gd increases. Thus, in the local area of the GDC, it finally forms a rare earth C-type structure at $x \geq 0.4$[25].

As we can see in Figure 6, for LDC, the curves of the second neighboring La-(La, Ce) and Ce-(La, Ce) distances are not synchronous with each other when x increases. The second neighboring distance comprises the distances Ln-Ln and Ln-Ce[27]. For LDC, the second neighboring La-(La, Ce) distance is first maintained (x = 0.1–0.4) and then slightly decreases (x = 0.5). This is because the local structure of La-O is more stable than that of Ce, and thus, the oxygen vacancies always surround Ce. The La-(La, Ce) distance is then stable and the Ce-(La, Ce) distance shortens with an increase in La. At the early stage of

La doping, the distance contribution of the La-La pairs is extremely small. The distance of the Ce-Ce pairs accounts for the majority, and Ce can maintain the 8-fold coordination due to charge compensation. With an increase in La doping, the La-La pairs gradually play a key role in the neighboring distance. Thus, the distance becomes stable at approximately 3.857 Å (x = 0.3–0.4), whereas the distance of the Ce-Ce pairs changes significantly because Ce changes from an 8-fold coordination to a 6-fold coordination. Moreover, the second neighboring Ce-(La, Ce) distance shortens gradually with an increase in the La doping amount (x = 0.2–0.5).

By contrast, for GDC, similar to the first stage of the La-(La, Ce) second neighboring distance, the distances of Gd-(Gd, Ce) and Ce-(Gd, Ce) first increase gradually (x = 0.1–0.2). However, they then decrease simultaneously with Gd doping. This is because the local Gd-O structure is not as stable in GDC as La-O is in LDC. The oxygen vacancies occur around both Gd and Ce. Then, the Gd-(Gd, Ce) and Ce-(Gd, Ce) distances are both shortened with an increase in Gd.

Scheme 1 represents the identical model of LDC and GDC at x = 0.5 based on the XAFS results. According to the higher ability of La^{3+} to catch up with O^{2-}, the oxygen vacancies surrounding La^{3+} are more stable, while those surrounding Ce^{4+} are very mobile. On the contrary, for GDC, the oxygen vacancies are the same due to the similar ability of catching up with O^{2-}. As presented in Figure 8, when the La concentration is low (x = 0.1), the La atoms are surrounded by Ce metal atoms, making an encounter with other La atoms difficult. Thus, the neighboring distance increases for La, which has a larger ionic radius in the structure. When the La concentration gradually increases, the La atoms have a better chance to combine and stabilize. The curves of the second neighboring Gd-(Gd, Ce) and Ce-(Gd, Ce) distances become extremely synchronous when x increases.

Figure 7 shows the lattice constants of LDC and GDC and the alignment of the second proximity distance. LDC and GDC have a fluorite-type structure with a low doping amount. Because they are doped at a high amount, they are in an ideal position due to the similar fluorite-type structure, and cations are present in the face-centered cubic lattice. We can then calculate the lattice parameters and the Ln-Ln distance.

As Ln is doped in cerium oxide, the lattice parameter changes more gradually whereas all (Ce, Ln)-O and (Ce,Ln)-(Ce, Ln) distances decrease. At the early doping stage, the amount of Ln is small and the contribution of the Ln-Ln distance is not a major lattice parameter. Thus, the lattice parameter is close to the Ce-Ce distance. In other words, Ce-Ce bonds form the framework of the cubic structure. With gradual Ln doping, the contribution of the Ln-Ln distance increases; finally, these bonds become the main framework in the cubic structure. This indicates that our XAFS results can fit the XRD results extremely well. In addition, it explains the relationship between the structural change and lattice parameter, and provides a new way to combine the two methods together to obtain local structural information for target materials.

Figure 8 shows the electrical conductivities of $Ce_{1-x}Ln_xO_{2-\delta}$ (Ln = La, Gd) ($0 \leq x \leq 0.5$) in air. The electrical conductivity of $Ce_{1-x}Gd_xO_{2-\delta}$ was taken from [24]. According to the results obtained, we considered the relationship between the electric conductivities and local structure as follows.

For LDC, at the first stage of x = 0–0.1, La is introduced into the CeO_2 cubic structure and replaces one Ce atom. Because La has almost no opportunity to encounter other La atoms, there is a stable oxygen vacancy caused by the local structure between La and Ce, allowing O^{2-} to pass through. Thus, oxygen vacancies surrounded by Ce atoms occur. Due to the minute amount of La, the paths for oxygen access are not completely formed.

Thus, at the x = 0.1 stage, the main reason for the increase in conductivity is the increase in the amount of free oxygen vacancies.

At x = 0.1–0.3, when the amount of La increases, the oxygen vacancies caused by the local structural change in La increase but still cannot effectively form an oxygen access path. By contrast, the number of free oxygen vacancies clearly decreases. These two factors cause the conductivity to decrease from 0.1 to 0.3.

As with x = 0.2–0.3, the structure begins to change from fluorite to a superstructure and some oxygen access paths are formed as the rate of decrease becomes less sharp than for x = 0.1–0.2.

At x = 0.3–0.4, the amount of La continuously increases with the ordered degree of the superstructure. In addition, the stable oxygen vacancies increase, clearly forming an oxygen access path, which is the main reason why the conductivity increases from 0.3 to 0.4.

At x = 0.4–0.5, the ordered degree of the superstructure increases. The amount of free oxygen vacancies decreases, reducing the conductivity.

For GDC, the main factor affecting the conductivity is the number of oxygen vacancies. Thus, like the other materials that have a doped metal element, the number of oxygen vacancies first increases and then decreases with the doping of the metal element. When a large amount of Gd is doped, the order degree of the C-type structure increases, whereas the oxygen vacancies remain in a statistically distributed state. Thus, the conductivity of the GDC appears to first increase and then decrease.

4. Conclusion

The changes in the local structures of $Ce_{1-x}Ln_xO_{2-\delta}$ with Ln (La, Gd) doping were investigated. XAFS was successfully used to clarify the coordination environments around Ce and the dopants La and Gd.

For LDC, La coordination was maintained at 7, and Ce coordination decreased from 8 to 6. It was speculated that because a superstructure would be formed, similar to a pyrochlore-type structure, in LDC at x>0.3, the oxygen vacancies could be attracted by the larger La^{3+}.

For GDC, the coordination numbers for Gd and Ce decreased from 8 to 6. In the GDC, oxygen vacancies had no preference for Ce or Gd coordination.

These results explained the changes in the lattice parameters for both LDC and GDC. The local structure change model was designed, and the electric conductivity change at each stage of Ln (La, Gd) doping was explained.

These results can be applied to other materials in future studies.

References

[1] A. Choudhury, H. Chandra, A. Arora, Application of solid oxide fuel cell technology for power generation—A review, Renew. Sustain. Energy Rev. 20 (2013) 430–442. https://doi.org/10.1016/j.rser.2012.11.031

[2] E. D. Washsman, C. A. Marlowe, K. T. Lee, Role of solid oxide fuel cells in a balanced energy strategy, Energy Environ. Sci., 5 (2) (2012) 5498–5509. https://doi.org/10.1039/C1EE02445K

[3] G-L. Xiao, S-W. Wang, Y. Lin, Y-X. Zhang, K. An, F-L. Chen, Releasing metal

catalysts via phase transition: $(NiO)_{0.05}$-$(SrTi_{0.8}Nb_{0.2}O_3)_{0.95}$ as a redox stable anode material for solid oxide fuel cells, ACS Appl. Mater. Interfaces, 6 (2014) 19990–19996. https://doi.org/10.1021/am5055417

[4] K. Pei., H. Li., G. Zou., R. Yu., H. Zhao, X. Shen, L. Wang, Y. Song, D. Qiu, Detonation nanodiamond introduced into samarium doped ceria electrolyte improving performance of solid oxide fuel cell, J. Power Sources, 342 (2017) 515–520. https://doi.org/10.1016/j.jpowsour.2016.12.051

[5] L. Ilieva, G. Pantaleo, I. Ivanov, R. Nedyalkova, A. M. Venezia, Molecular structure Performance relationships at the surface of functional materials, Catal. Today 139 (2009) 168–173. https://doi.org/10.1016/j.cattod.2012.02.021

[6] M. Jamshidijam, P. Thangaraj, A. Akbari-Fakhrabadi, M. Angel, N. Galeano, J. Usuba, M. R. Viswanathan, Influence of rare earth (RE=Nd, Y, Pr and Er) doping on the microstructural and optical properties of ceria nanostructures, Ceram. Int., 43 (2017) 5216–5222. https://doi.org/10.1016/j.ceramint.2017.01.046

[7] K. Neuhaus, M. Grünebaum, M. Janssen, S. Baumann, F. Schulze-Küppers, H.-D. Wiemhöfer, Electronic conductivity of $Ce_{0.80}Gd_{0.2-x}Pr_xO_{2-\delta}$ and influence of added CoO, Phys. Stat. Sol., B 248 (2011) 314–322. https://doi.org/10.1002/pssb.201046365

[8] V. V. Kharton, A. P. Viskup, F. M. Figueiredo, E. N. Naumovich, A. A. Yaremchenko, F. M. B. Marques, Electron-hole conduction in Pr-doped $Ce(Gd)O_{2-\delta}$ by faradaic efficiency and emf measurements, Electrochim. Acta, 46 (2001) 2879–2889. https://doi.org/10.1016/S0013-4686(01)00505-9

[9] V. V. Kharton, A. P. Viskup, F. M. Figueiredo, E. N. Naumovich, A. L. Shaulo, F. M. B. Marques, Mater. Lett., 53 (2002) 160–164.

[10] S. Lubke, H.-D. Wiemhofer, Electronic conductivity of Gd-doped ceria with

additional Pr-doping, Solid State Ionics, 117 (1999) 229–243. https://doi.org/10.1016/S0167-2738(98)00408-1

[11] S. Cheng, C. Chatzichristodoulou, M. Søgaard, A. Kaiser, P. V. Hendriksen, Ionic/electronic conductivity, thermal/chemical expansion and oxygen permeation in Pr and Gd Co-Doped Ceria $Pr_xGd_{0.1}Ce_{0.9-x}O_{1.95-\delta}$, J. Electrochem. Soc., 164 (2017) F1354–F1367. https://doi.org/10.1149/2.0531713jes

[12] R. Bhosale, G.D. Takalkar, Nanostructured co-precipitated $Ce_{0.9}Ln_{0.1}O_2$ (Ln = La, Pr, Sm, Nd, Gd, Tb, Dy, or Er) for thermochemical conversion of CO_2, Ceram. Int., 44 (2018) 16688–16697. https://doi.org/10.1016/j.ceramint.2018.06.096

[13] B. C. H. Steele, Appraisal of $Ce_{1-y}Gd_yO_{2-y/2}$ electrolytes for IT-SOFC operation at 500°C, Solid State Ionics, 129 (2000) 95–110. https://doi.org/10.1016/S0167-2738(99)00319-7

[14] M. Mori, H. Sumi, E. Suda, Evaluation of $Ce_{1-x}La_xO_{2-\delta}$-based ceria ($0 \leq x \leq 0.5$) as cell components in electrochemical cells, Abstract for the Ceramic Society of Japan the 29th Fall Meeting, 1PV01 (2016).

[15] H. Yamamura, H. Nishino, K. Kakinuma, K. Nomura, Electrical conductivity anomaly around fluorite–pyrochlore phase boundary, Solid State Ionics, 158 (2003) 359–365. https://doi.org/10.1016/S0167-2738(02)00874-3

[16] L. Kalland, S. T. Norberg, J. Kyrklund, S. Hull, S. G. Eriksson, T. Norby, C. E. Mohn, C. S. Knee, C-type related order in the defective fluorites $La_2Ce_2O_7$ and $Nd_2Ce_2O_7$ studied by neutron scattering and ab initio MD simulations, Phys. Chem. Chem. Phys., 18, (2016) 24070–24080. https://doi.org/10.1039/C6CP04708D

[17] E. Suda, B. Pacaud, Y. Montardi, M. Mori, M. Ozawa, Y. Takeda, Low-temperature sinterable $Ce_{0.9}Gd_{0.1}O_{1.95}$ Powder synthesized through newly-devised heat-treatment in

the coprecipitation process, Electrochemistry, 71 (2003) 866–872.

[18] R. D. Shannon, Revised effective ionic radii and systematic studies of interatomic distances in halides and chalcogenides, Acta Cryst. A32 (1976) 751–767. https://doi.org/10.1107/S0567739476001551

[19] B. Ravel, M. Newville, ATHENA, ARTEMIS, HEPHAESTUS: Data analysis for X-ray absorption spectroscopy using IFEFFIT, J. Synchrotron Rad., 12 (2005) 537–541. https://doi.org/10.1107/S0909049505012719

[20] X. Li, Z. Feng, J. Lu, F. Wang, M. Xue, G. Shao, Synthesis and electrical properties of $Ce_{1-x}Gd_xO_{2-x/2}$ (x = 0.05–0.3) solid solutions prepared by a citrate–nitrate combustion method, Ceram. Int., 38 (2012) 3203–3207. https://doi.org/10.1016/j.ceramint.2011.12.025

[21] J. Zhang, C. Ke, H. Wu, J. Wang, Y. Wang, Solubility limits, crystal structure and lattice thermal expansion of Ln_2O_3 (Ln=Sm, Eu, Gd) doped CeO_2, J. Alloys Compd., 718 (2017) 85–91. https://doi.org/10.1016/j.jallcom.2017.05.073

[22] S. Yamazaki, T. Matsui, Structure and high temperature thermophysical properties of pyrochlore-type oxides, Netsu Sokutei, 26 (1999) 82–91. https://doi.org/10.11311/jscta1974.26.82

[23] D. Seo, K. Ryu, S. Park, K. Kim, R. Song, Synthesis and properties of $Ce_{1-x}Gd_xO_{2-x/2}$ solid solution prepared by flame spray pyrolysis, Mater. Res. Bull., 41 (2006) 359–366. https://doi.org/10.1016/j.materresbull.2005.08.012

[24] R. D. Shannon, Revised effective ionic radii and systematic studies of interatomic distances in halides and chalcogenides, Acta Cryst. A32 (1976) 751–767. https://doi.org/10.1107/S0567739476001551

[25] M. Nolan, Charge compensation and Ce^{3+} formation in trivalent doping of the CeO_2(110) surface: The key role of dopant ionic radius, J. Phys. Chem. C, 115 (2011) 6671–6681. https://doi.org/10.1021/jp112112u

[26] L. Pauling, The nature of the chemical bond-1992, J. Chem. Educ. 69 (1992) 519. https://doi.org/10.1021/ed069p519

[27] H. Deguchi, H. Yoshida, T. Inagaki, M. Horiuchi, EXAFS study of doped ceria using multiple data set fit, Solid State Ionics 176 (2005) 1817–1825. https://doi.org/10.1016/j.ssi.2005.04.043

Figure Captions

Figure 1 Conductivity for different doping amounts in LDC materials [14].

Table 1 XAFS analysis conditions and obtained parameters for the first shell of LDC and GDC.

Table 2 XAFS analysis conditions and obtained parameters for the second shell of LDC and GDC.

Figure 2 Lattice parameters of $Ce_{1-x}Ln_xO_{2-\delta}$ (Ln = La, Gd) ($0 \leq x \leq 0.5$).

Figure 3 XANES spectra near the Ce K, La K, and Gd K of $Ce_{1-x}La_xO_{2-\delta}$ and $Ce_{1-x}Gd_xO_{2-\delta}$.

Figure 4 Fourier transforms (FTs) of k^3-weighted EXAFS oscillation of LDC and GDC.

Figure 5 Ln-O inter atomic distance in $Ce_{1-x}Ln_xO_{2-\delta}$ ($0 \leq x \leq 0.5$) (Ln = La, Gd).

Figure 6 Ln-Ln inter atomic distance in $Ce_{1-x}Ln_xO_{2-\delta}$ ($0 \leq x \leq 0.5$) calculated by second shell (Ln = La, Gd).

Scheme 1 Identical model of LDC and GDC at x = 0.5.

Figure 7 Ln-Ln inter atomic distance in $Ce_{1-x}Ln_xO_{2-\delta}$ ($0 \leq x \leq 0.5$) calculated by second

shell (Ln=La, Gd).

Figure 8 Electrical conductivities of $Ce_{1-x}Ln_xO_{2-\delta}$ (Ln = La, Gd) ($0 \leq x \leq 0.5$) in air.

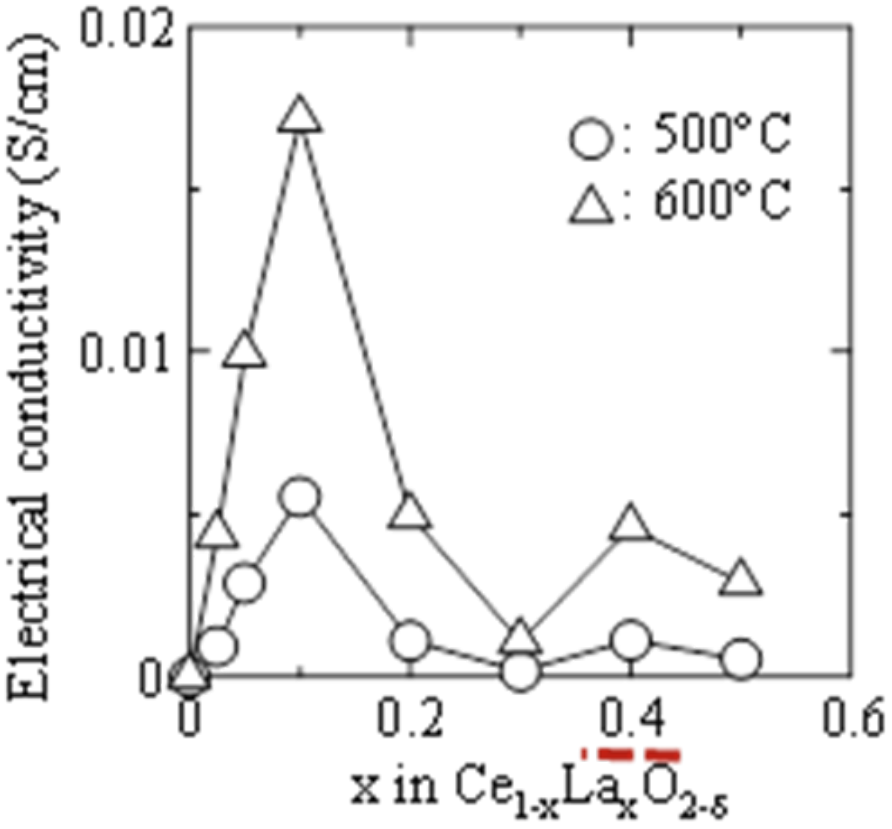
Electrical conductivity (S/cm)
0.02
0.01
0
0
0.2
0.4
0.6
○: 500°C
△: 600°C
x in Ce1-xLaxO2-δ

Figure 1

			N	S02	E0	R	δ2	R-factor
LDC	La K-edge	0	8	1.816±0.368	-9.439±2.840	2.353±0.014	0.008±0.002	0.0041
		0.1	8	1.627±0.360	-5.625±2.895	2.458±0.018	0.008±0.002	0.010
		0.2	8	1.729±0.238	-6.421±1.781	2.463±0.012	0.010±0.001	0.0036
		0.3	8	1.739±0.242	-3.687±1.794	2.463±0.013	0.01110.002	0.0035
		0.4	8	1.562±0.349	-7.387±2.880	2.460±0.020	0.011±0.002	0.0087
		0.5	8	1.440±0.312	-8.690±2.822	2.450±0.019	0.011±0.002	0.0084
	Ce K-edge	0	8	1.816±0.368	-9.439±2.840	2.353±0.014	0.008±0.001	0.0041
		0.1	8	1.794±0.211	-7.533±1.656	2.339±0.009	0.010±0.001	0.0029
		0.2	8	1.715±0.228	-9.890±1.932	2.318±0.011	0.011±0.001	0.0015
		0.3	8	1.686±0.254	-15.280±2.192	2.295±0.011	0.011±0.001	0.0018
		0.4	8	1.677±0.246	-11.889±2.195	2.285±0.012	0.012±0.001	0.0017
		0.5	8	1.755±0.202	-12.497±1.750	2.268±0.009	0.012±0.001	0.0010

			N	S02	E0	R	Δ2	R-factor
GDC	Gd K-edge	0	8	1.810±0.368	-9.439±2.840	2.353±0.014	0.008±0.001	0.0041
		0.1	8	1.326±0.546	-1.318±5.231	2.391±0.032	0.010±0.004	0.0227
		0.2	8	1.342±0.439	-2.259±4.269	2.364±0.024	0.008±0.003	0.0154
		0.3	8	1.261±0.422	-10.150±4.527	2.350±0.023	0.007±0.002	0.0119
		0.4	8	1.173±0.436	-11.505±5.089	2.348±0.026	0.007±0.003	0.0060
		0.5	8	1.051±0.449	-5.034±5.689	2.341±0.030	0.006±0.003	0.0082
	Cd K-edge	0	8	1.816±0.368	-9.439±2.840	2.353±0.014	0.007±0.001	0.0041
		0.1	8	1.354±0.630	-0.992±5.832	2.394±0.037	0.001±0.004	0.0283
		0.2	8	1.342±0.439	-2.259±4.269	2.364±0.024	0.008±0.003	0.0154
		0.3	8	1.272±0.385	0.008±0.003	2.351±0.021	-9.951±3.997	0.0127
		0.4	8	1.183±0.269	-11.575±3.052	2.348±0.015	0.007±0.002	0.0072
		0.5	8	1.090±0.309	-5.099±3.761	2.341±0.019	0.007±0.002	0.0118

Table 1

	absorbing atom	scattering atom	composition	N	S02	E0	R	δ2	R-factor
LDC	La	La	0	0	-	-	-	-	-
			0.1	1.2	5.832±3.991	-49.165±6.650	3.972±0.017	0.003±0.001	0.008
			0.2	2.4	14.899±15.547	5.366±7.731	3.957±0.118	0.026±0.016	0.004
			0.3	3.6	8.805±3.609	-12.316±9.656	3.964±0.008	0.006±0.001	0.065
			0.4	4.8	4.154±2.106	-12.411±4.260	3.960±0.004	0.008±0.001	0.021
			0.5	6	7.392±5.333	-3.448±4.739	3.940±0.026	0.012±0.003	0.006
		Ce	0	12	-	-	-	-	-
			0.1	10.8	3.274±1.704	-3.152±4.166	3.896±0.041	0.013±0.004	0.008
			0.2	9.6	2.087±0.594	-12.290±2.476	3.853±0.008	0.007±0.001	0.004
			0.3	8.4	5.621±19.455	-1.958±6.211	3.873±0.136	0.006±0.009	0.065
			0.4	7.2	3.914±14.503	-5.005±3.465	3.865±0.146	0.008±0.012	0.021
			0.5	6	3.229±3.688	8.409±7.695	3.862±0.025	0.010±0.003	0.006
	Ce	La	0	0	-	-	-	-	-
			0.1	1.2	3.274±1.704	0.225±28.297	3.896±0.041	0.013±0.004	0.012
			0.2	2.4	2.087±0.594	-21.314±37.558	3.853±0.008	0.007±0.001	0.024
			0.3	3.6	5.621±19.455	-11.137±50.831	3.873±0.136	0.006±0.009	0.024
			0.4	4.8	3.914±14.503	-8.246±54.036	3.865±0.146	0.008±0.012	0.034
			0.5	6	3.229±3.688	-9.076±10.291	3.862±0.025	0.010±0.003	0.030
		Ce	0	12	-	-	-	-	-
			0.1	10.8	1.653±1.124	-13.039±1.960	3.837±0.015	0.006±0.002	0.012
			0.2	9.6	2.109±3.069	-11.077±7.629	3.833±0.036	0.009±0.002	0.024
			0.3	8.4	0.707±5.883	0.172±126.236	3.786±0.289	0.003±0.019	0.024
			0.4	7.2	0.719±6.541	3.039±143.315	3.783±0.281	0.004±0.022	0.034
			0.5	6	1.119±1.508	1.009±21.066	3.781±0.039	0.006±0.003	0.030

	absorbing atom	scattering atom	composition	N	S02	E0	R	δ2	R-factor
GDC	Gd	Gd	0	0	-	-	-	-	-
			0.1	1.2	40.625±55.241	-2.001±9.770	3.993±0.072	0.011±0.006	0.003
			0.2	2.4	5.427±12.783	0.978±11.823	3.925±0.072	0.006±0.013	0.004
			0.3	3.6	4.221±7.813	-7.049±12.120	3.906±0.047	0.007±0.009	0.004
			0.4	4.8	7.181±5.059	-7.058±5.608	3.850±0.060	0.018±0.011	0.110
			0.5	6	0.994±0.840	-44.575±8.590	3.838±0.033	0.005±0.003	0.067
		Ce	0	12	-	-	-	-	-
			0.1	10.8	3.719±4.318	7.079±7.892	3.881±0.047	0.009±0.005	0.003
			0.2	9.6	1.074±2.815	6.818±12.947	3.830±0.080	0.004±0.013	0.004
			0.3	8.4	1.737±3.509	0.048±10.131	3.806±0.049	0.006±0.010	0.004
			0.4	7.2	0.697±0.517	1.888±11.298	3.794±0.041	0.007±0.003	0.110
			0.5	6	0.963±0.889	1.942±7.438	3.810±0.043	0.013±0.007	0.067
	Ce	Gd	0	0	-	-	-	-	-
			0.1	1.2	3.719±4.318	-5.023±10.177	3.881±0.047	0.009±0.005	0.010
			0.2	2.4	1.074±2.815	-32.092±21.350	3.830±0.080	0.004±0.013	0.021
			0.3	3.6	1.737±3.509	-43.570±18.188	3.806±0.049	0.006±0.010	0.089
			0.4	4.8	0.697±0.517	31.930±4.399	3.794±0.041	0.007±0.003	0.003
			0.5	6	0.963±0.889	35.886±4.837	3.810±0.043	0.013±0.007	0.002
		Ce	0	12	-	-	-	-	-
			0.1	10.8	1.383±0.351	-15.586±2.314	3.832±0.006	0.005±0.001	0.010
			0.2	9.6	1.949±0.374	-11.336±2.178	3.817±0.011	0.007±0.001	0.021
			0.3	8.4	2.187±0.656	-20.524±3.895	3.777±0.021	0.008±0.001	0.089
			0.4	7.2	0.995±0.437	-13.686±2.630	3.772±0.019	0.006±0.001	0.003
			0.5	6	1.154±0.321	-13.529±2.406	3.743±0.012	0.006±0.001	0.002

Table 2

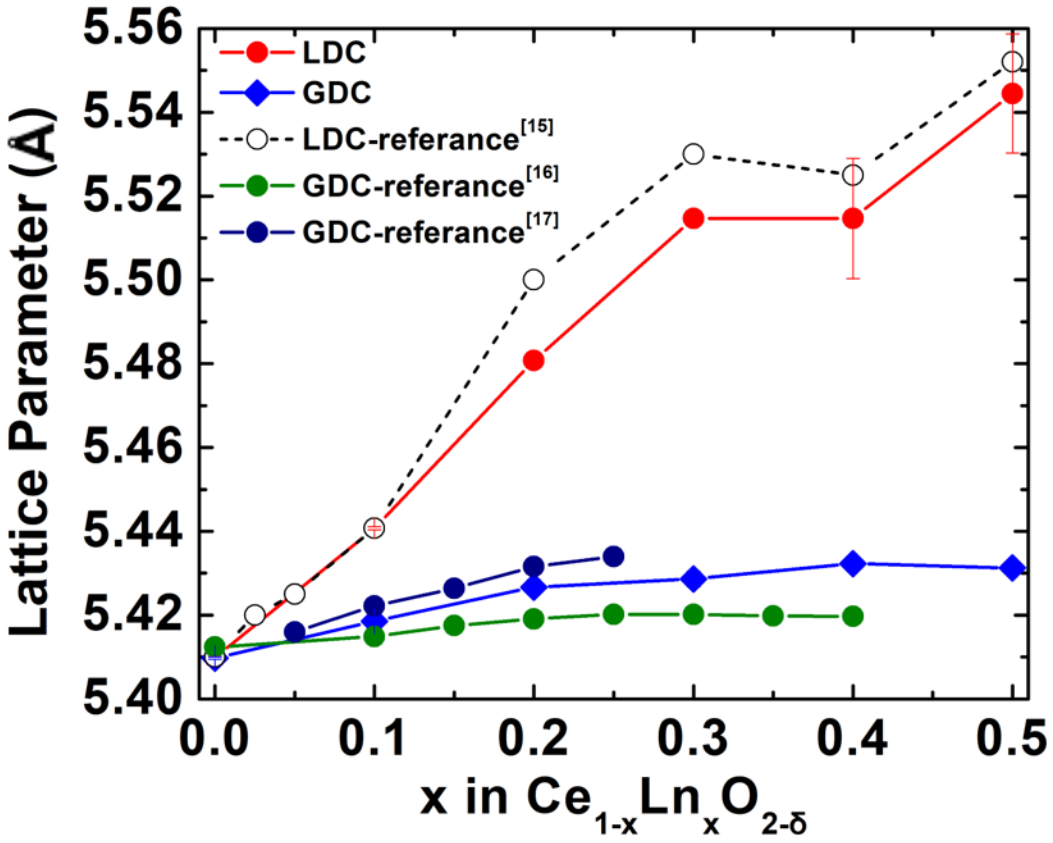
Lattice Parameter (Å)
5.56
5.54
5.52
5.50
5.48
5.46
5.44
5.42
5.40
0.0
0.1
0.2
0.3
0.4
0.5
x in Ce1-xLnxO2-δ
LDC
GDC
LDC-referance[15]
GDC-referance[16]
GDC-referance[17]

Figure 2

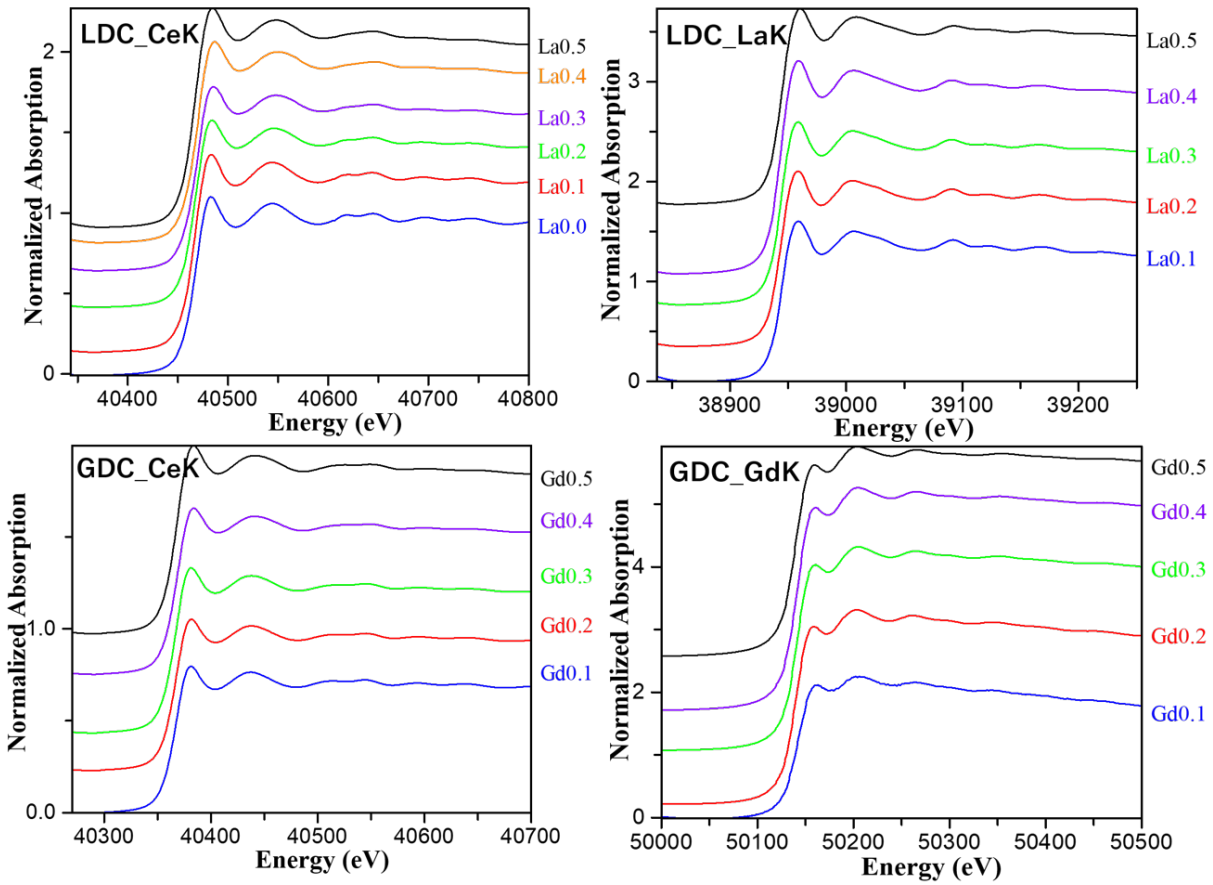
LDC_CeK
La0.5
La0.4
La0.3
La0.2
La0.1
La0.0
Normalized Absorption
Energy (eV)
LDC_LaK
La0.5
La0.4
La0.3
La0.2
La0.1
Normalized Absorption
Energy (eV)
GDC_CeK
Gd0.5
Gd0.4
Gd0.3
Gd0.2
Gd0.1
Normalized Absorption
Energy (eV)
GDC_GdK
Gd0.5
Gd0.4
Gd0.3
Gd0.2
Gd0.1
Normalized Absorption
Energy (eV)

Figure 3

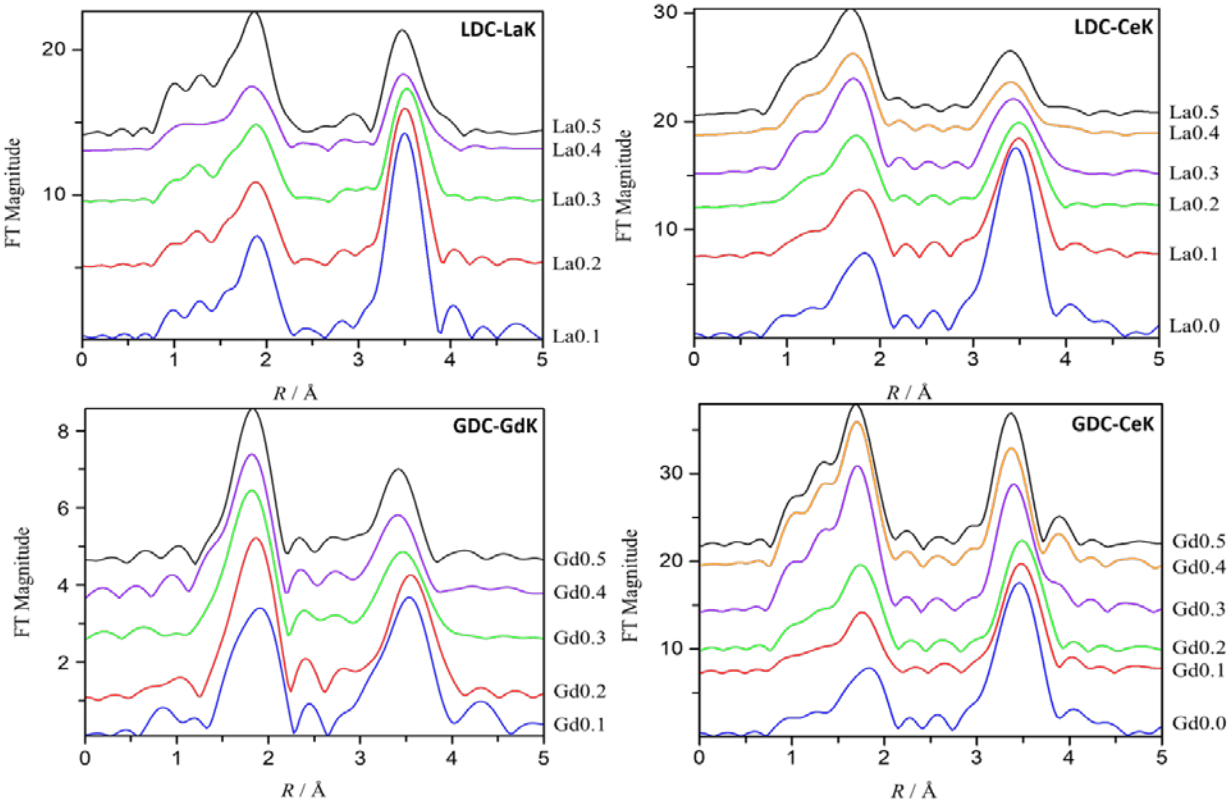
LDC-LaK
La0.5
La0.4
La0.3
La0.2
La0.1
LDC-CeK
La0.5
La0.4
La0.3
La0.2
La0.1
La0.0
GDC-GdK
Gd0.5
Gd0.4
Gd0.3
Gd0.2
Gd0.1
GDC-CeK
Gd0.5
Gd0.4
Gd0.3
Gd0.2
Gd0.1
Gd0.0
FT Magnitude
R / Å

Figure 4

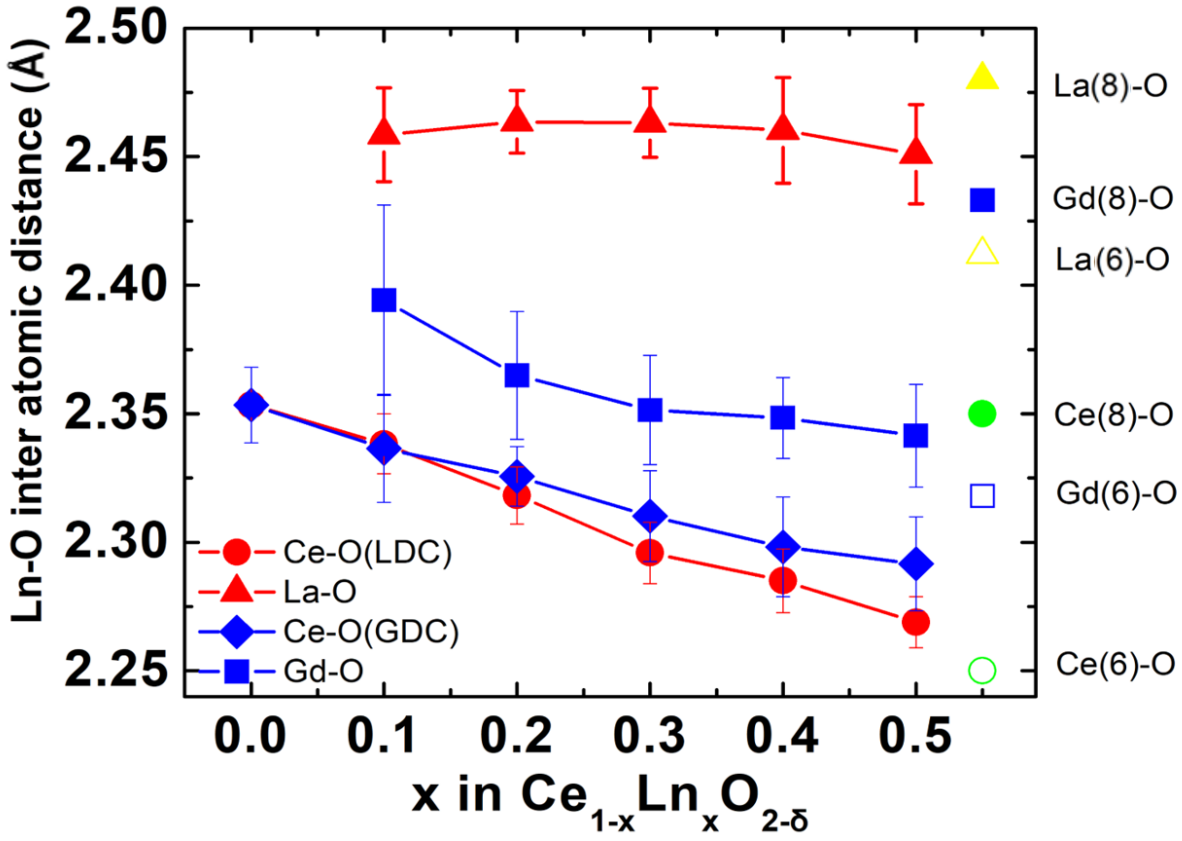
Ln-O inter atomic distance (Å)
2.50
2.45
2.40
2.35
2.30
2.25
0.0
0.1
0.2
0.3
0.4
0.5
x in Ce1-xLnxO2-δ
Ce-O(LDC)
La-O
Ce-O(GDC)
Gd-O
La(8)-O
Gd(8)-O
La(6)-O
Ce(8)-O
Gd(6)-O
Ce(6)-O

Figure 5

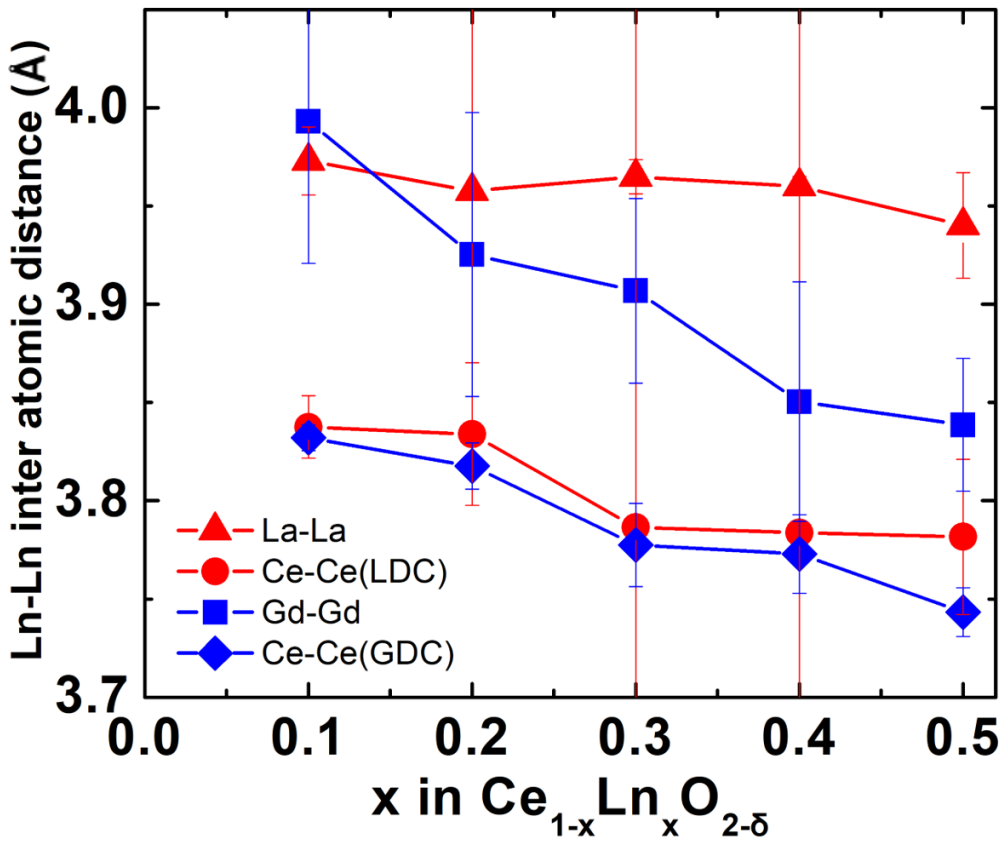
Ln-Ln inter atomic distance (Å)
4.0
3.9
3.8
3.7
0.0
0.1
0.2
0.3
0.4
0.5
x in Ce1-xLnxO2-δ
La-La
Ce-Ce(LDC)
Gd-Gd
Ce-Ce(GDC)

Figure 6

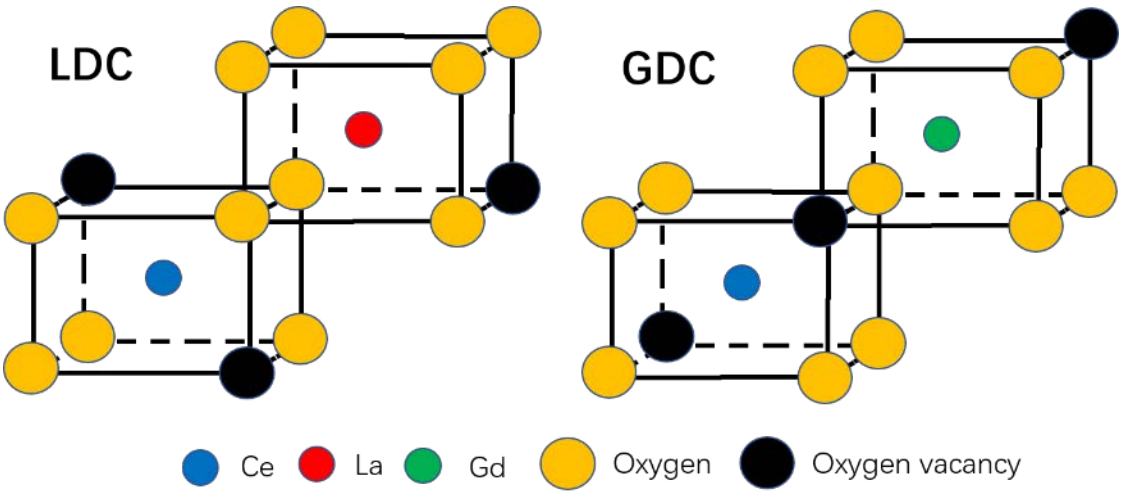

Scheme 1

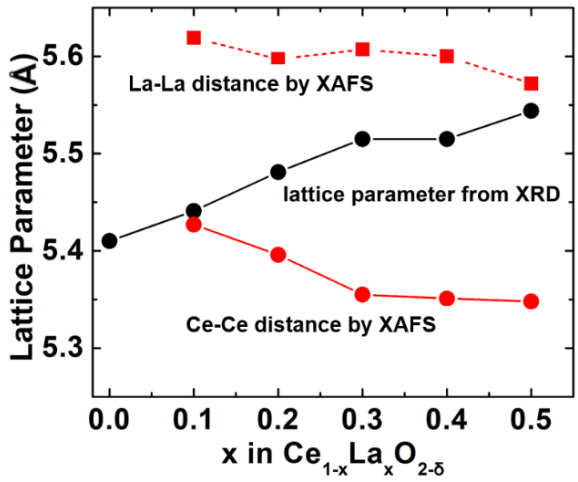
Lattice Parameter (Å)
5.6
5.5
5.4
5.3
La-La distance by XAFS
lattice parameter from XRD
Ce-Ce distance by XAFS
0.0
0.1
0.2
0.3
0.4
0.5
x in Ce1-xLaxO2-δ

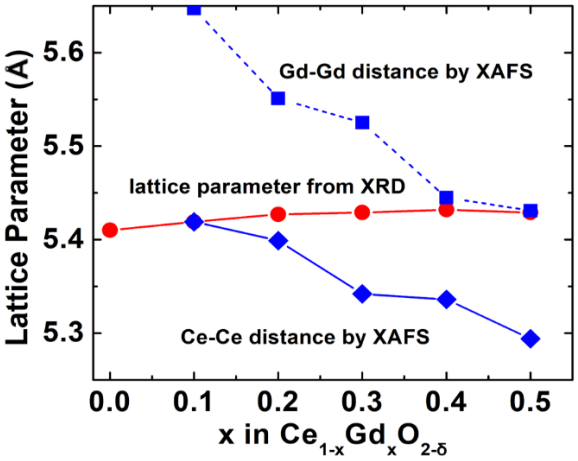
Lattice Parameter (Å)
5.6
5.5
5.4
5.3
Gd-Gd distance by XAFS
lattice parameter from XRD
Ce-Ce distance by XAFS
0.0
0.1
0.2
0.3
0.4
0.5
x in Ce1-xGdxO2-δ

Figure 7

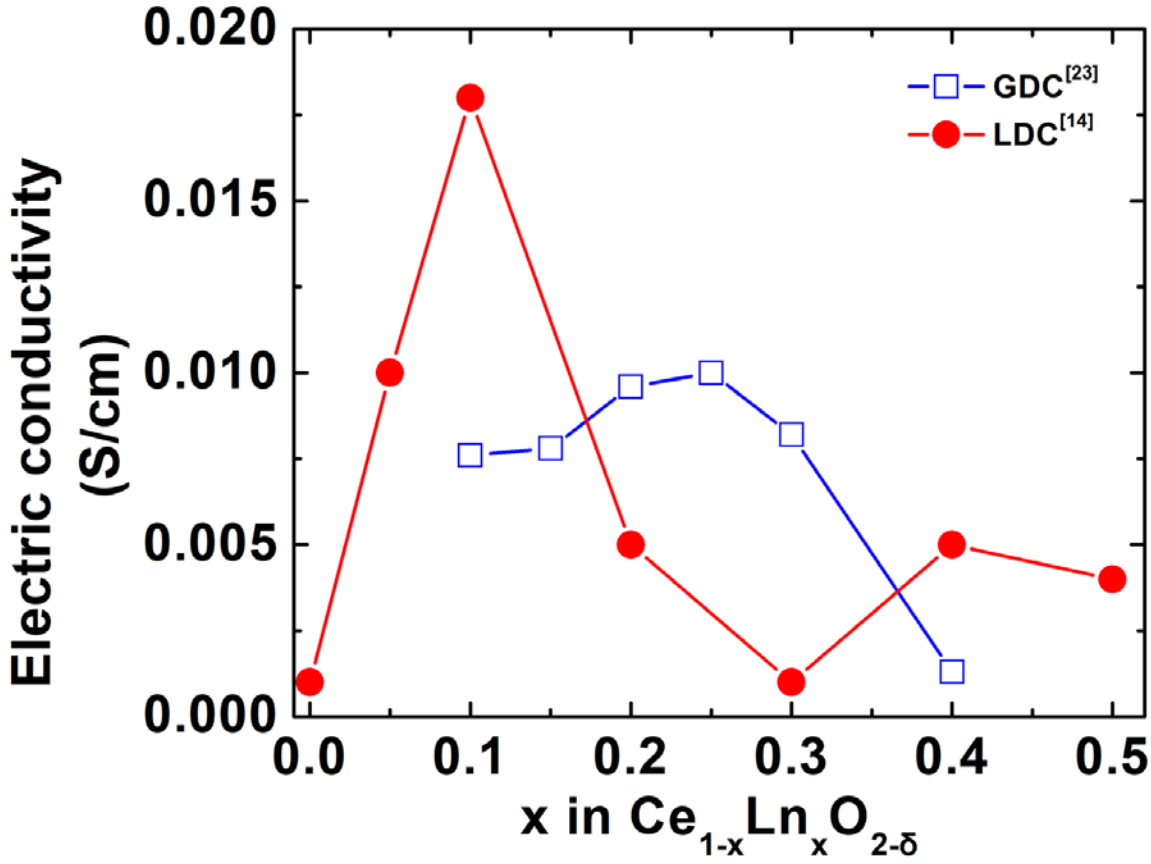
Electric conductivity (S/cm)
0.020
0.015
0.010
0.005
0.000
0.0
0.1
0.2
0.3
0.4
0.5
x in Ce1-xLnxO2-δ
GDC[23]
LDC[14]

Figure 8

Figure 1 The conductivity of different doping amount in LDC material[14].

Table 1 XAFS analysis condition and obtained parameters of 1st shell for LDC and GDC.

Table 2 XAFS analysis condition and obtained parameters of 2nd shell for LDC and GDC.

Figure 2 The lattice parameters of $Ce_{1-x}Ln_xO_{2-\delta}$ (Ln=La, Gd) ($0 \leqq x \leqq 0.5$).

Figure 3 The EXAFS spectra near the CeK, LaK and GdK of $Ce_{1-x}La_xO_{2-\delta}$ and $Ce_{1-x}Gd_xO_{2-\delta}$.

Figure 4 Fourier transforms (FTs) of k3-weighted EXAFS oscillation of LDC and GDC.

Figure 5 Ln-O inter atomic distance in $Ce_{1-x}Ln_xO_{2-\delta}$ ($0 \leqq x \leqq 0.5$) (Ln=La, Gd).

Figure 6 Ln-Ln inter atomic distance in $Ce_{1-x}Ln_xO_{2-\delta}$ ($0 \leqq x \leqq 0.5$) calculated by 2 shell (Ln=La, Gd).

Scheme 1 The identical model of LDC and GDC at x=0.5.

Figure 7 Ln-Ln inter atomic distance in $Ce_{1-x}Ln_xO_{2-\delta}$ ($0 \leqq x \leqq 0.5$) calculated by 2 shell (Ln=La, Gd).

Figure 8 Electric conductivities of $Ce_{1-x}Ln_xO_{2-\delta}$(Ln=La, Gd)($0 \leqq x \leqq 0.5$) in the air.